Effect of sample thinning on strains and lattice rotations measured from Transmission Kikuchi Diffraction in the SEM

Phani S. Karamched*, Naganand Saravanan, Jack C. Haley, Angus J. Wilkinson and Sergio Lozano-Perez

Department of Materials, University of Oxford, Parks Road, Oxford – OX1 3PH

Abstract

Cross correlation based high angular resolution EBSD (or HR-EBSD) has been developed for measurement of elastic strains, lattice rotations (and estimating GND density). Recent advances in Transmission Kikuchi diffraction (TKD), especially the on-axis geometry allows the possibility of acquiring patterns at higher spatial resolution. However, some controversy remains as to whether stresses/strains measured after the sample thinning process are still representative of the bulk sample. In this paper, we explore a way of applying the HR-EBSD method to study strains and lattice rotations in an initially bulk sample, that is then progressively thinned down until a similar analysis can be performed on thin (and electron transparent) samples. Thus, HR-TKD will be compared as a possible alternative to HR-EBSD, in scenarios when it is not always possible to perform EBSD on the surface of the sample. An estimate of strain relaxation in the sample as a result of sample thinning is presented.

Keywords: HR-EBSD, HR-TKD, on-axis TKD, thin sample, Transmission Kikuchi Diffraction

*Corresponding author
Email address: phani.karamched@materials.ox.ac.uk (Phani S. Karamched)

1. Introduction

Electron backscattered Diffraction (EBSD) is an SEM based technique that is essentially based on capturing and analysing Kikuchi patterns to measure crystal orientations. These relatively simple-to-measure details (crystal type and orientation) using this method have unleashed huge capabilities, making it a ubiquitous tool for quantitative microstructural characterisation (grain shapes and sizes, phase distribution, recrystallisation, orientation relationship, types of grain and phase boundaries, microtexture) in bulk samples. These applications have been reviewed in the past [1, 2, 3, 4] and more recently the novel applications [5, 6]. Building on the simple Hough based analysis on the Kikuchi patterns was the high-angular resolution EBSD (HR EBSD) method, a cross-correlation based analysis of Kikuchi patterns, that is often performed off-line after data acquisition [7, 8]. This technique has been implemented and improved by several research groups in recent years [9, 10, 11, 12, 13, 14, 15] to measure elastic strain distributions, lattice rotations (compared to a reference pattern) and estimating a Geometrically Necessary Dislocation (GND) density using Nye's tensor framework [16].

About a decade ago a technique similar to EBSD but in transmission was introduced as Transmission Kikuchi Diffraction (TKD, also referred as t-EBSD) in the SEM [17, 18] for thin samples. Quite soon after this method became popular due to significantly better spatial resolution [17, 19]. More recently, a new hardware setup was introduced [20], where the phosphor screen in the setup is parallel to the plane of the thin sample and directly underneath. This setup, known as on-axis TKD, has an added advantage of obtaining Kikuchi patterns with much lesser gnomonic distortion than the t EBSD setup, higher signal levels and consequently less sensitive to beam drift [21, 22] due to shorter scan times.

A similar cross-correlation approach can be used as in HR-EBSD to measure shifts and rotations in TKD patterns, thereby extending the ability of the technique [22]. In addition to this, the forescatter (FSD) diodes on the setup

can be used to obtain TEM like Bright-Field and Dark-Field images [23] to a point where dislocations and their pile-ups are clearly visible [22]. This cross-correlation approach (HR-TKD in this case), can be used to measure strain and rotation fields (thereby a GND density estimation for deformation) in small areas not accessible by traditional EBSD, via a site-specific FIB liftout or by electropolishing [22]. An example of the potential of this technique is for the study of localised deformation around crack tips (especially in stress corrosion cracking, where the cracks are sub-surface) [24, 25] or around smaller microstructural features that need a high spatial resolution for imaging/measurement [26]. However, a question that remains to be answered is if the measurements are still representative of the bulk sample and if the stresses and strains have relaxed from thinning the sample by FIB preparation.

In this paper, we report the elastic strain and lattice rotation measurements obtained from a thick sample (in EBSD) which is then progressively thinned with a FIB instrument to a point where the sample is electron transparent and TKD patterns can be obtained in an on-axis TKD setup. Cross correlation analysis of the obtained patterns has been used to compute the elastic strains and rotations from the bulk and thinned sample. We also make an estimate of the loss of strain due to relaxation in the thin sample.

2. Experimental method

The material selected for this study is a sample of Alloy 600, a Ni-based alloy and its composition listed in Table 1. The material was solution annealed for 30 minutes at 1150°C and water quenched. This specimen was cut into smaller pieces and then the surface was ground with SiC paper and polished with 1 μm diamond suspension. This sample was then further polished in a suspension of colloidal silica (50-60 nm).

A Zeiss Crossbeam 540 FIB-SEM was subsequently used for lifting-out a sample containing the mapped area of interest within a single grain, cross-sectionally to the surface of the polished sample. The initial lift-out sample

C	Mn	Si	Ni	Cr	Al	Ti	Fe	Cu	S	P
0.07	0.17	0.29	73.6	16.3	0.19	0.19	9.20	0.01	<0.001	<0.007

Table 1: Chemical composition of the selected Alloy-600 (in wt%)

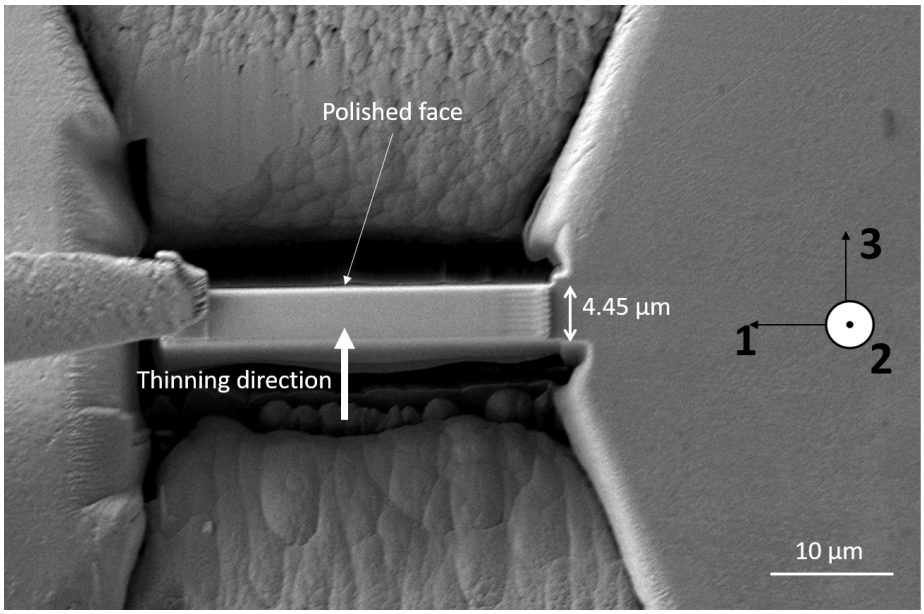

Figure 1: Initial sample lift-out. Sample S1 showing the thickness, polished face and the thinning direction.

was $\sim 5\mu$m thick. This lift-out was then placed on a copper Omniprobe^{TM} grid. One of its surfaces was then polished in the FIB (for EBSD) to a thickness of $\sim 4.5\mu$m with a 300pA@30KV beam and then with 200pA@5KV to minimise damage from FIB milling. This sample (S1) before being placed on the copper grid is shown in Figure 1, depicting the initial thickness, polished face for EBSD map and the thinning direction.

An EBSD map was acquired (5nA@20KV) from the bulk sample on the polished surface using a Bruker e-Flash^{HD} detector at a pattern resolution of 800×600 pixels. These conditions were chosen to be an acceleration voltage of 20KV and a probe current of 5nA to match those where a 50nm step size (an spatial resolution) could be confidently obtained as demonstrated by Bordín

et al. [27]. This sample was then thinned on the opposite side using the FIB (1nA@30KV) until a thickness of $\sim 1\mu$m to prepare the sample S2. The sample was not cleaned in any other way for S2. Another EBSD map was acquired and the sample re-thinned using the FIB (300pA@30KV) followed by 200pA@5KV until the sample was electron transparent with the secondary electron detector at 10KV. The sample thickness in this condition was estimated to be 110-135nm, from a series of high magnification images stitched together. This sample was designated S3 and TKD patterns acquired, with the polished face on the exit side, using the same detector, but with the on-axis OPTIMUS$^{\text{TM}}$ detector head at 800×600 pattern resolution. The patterns were obtained at an acceleration voltage of 30KV and a probe current of 1nA. Probe currents larger than 2.5nA often result in containments from the chamber being deposited on the sample as a layer, rendering it unsuitable for any high resolution TEM studies. It was observed that the sample started to bend at this stage. A fourth sample was then prepared by further thinning it with the FIB beam (200pA@5KV), to study the strains from the resulting bending. This sample is designated as sample S4. The thickness of the sample at this stage was found to be 70-90 nm. The general trend to prepare TKD samples is normally to a thickness of 100nm (sample S3). The sample S4 was prepared (upon suggestion from reviewers) to understand the bending issues and the strains related to measure this effect. A summary of the samples is presented in Table 2. Although S1, S2, S3 and S4 are the same sample and EBSD/TKD mapped surface stays the same, they have been designated with a different sample number for identification purposes.

The lift-out was intentionally placed on the V-shaped post of the Omniprobe$^{\text{TM}}$ grid. This was done to remove shadowing during TKD acquisition, as it was seen that placing the sample on the vertical bar results in shadows in the obtained patterns while mapping an area close to the post with on-axis TKD setup. Also, this method was intended to minimise the stress/strain relaxation in the plane of the sample by having the sample welded on both sides. The resulting thin sample (S3) is shown in Figure 2. Previous experience with preparing samples attached to a vertical bar in the grid (welded on just one side) resulted in too

Sample designation	**Thickness**	**EBSD/TKD mode**	**Microscope conditions for acquisition**	**Pattern resolution (pixels)**	**Spatial Resolution (approximate)**
S1	4.5μm	EBSD (50nm stepsize)	20KV, 5nA	800 × 600	50nm
S2	1μm	EBSD (50nm stepsize)	20KV, 5nA	800 × 600	50nm
S3	110-135nm	On-axis TKD (50nm stepsize)	30KV, 1nA	800 × 600	<5nm
S4	70-90nm	On-axis TKD (50nm stepsize)	30KV, 1nA	800 × 600	<5nm

Table 2: Sample summary of the thickness, conditions and mode of Kikuchi pattern acquisition.

much sample bending and hence this method of preparation was preferred for TKD.

The patterns obtained from EBSD and on-axis TKD were subjected to cross-correlation based measurement of pattern shifts using an in-house developed MATLAB code [15] across ∼20 ROIs and elastic strains and lattice rotations measured. Each ROI was extracted from the reference and test pattern and filtered to remove high-frequency noise and long-range gradients [28]. Sufficient care was taken to exclude the central area in the TKD patterns where the direct beam saturates the pixels on the detector. The patterns from EBSD and TKD

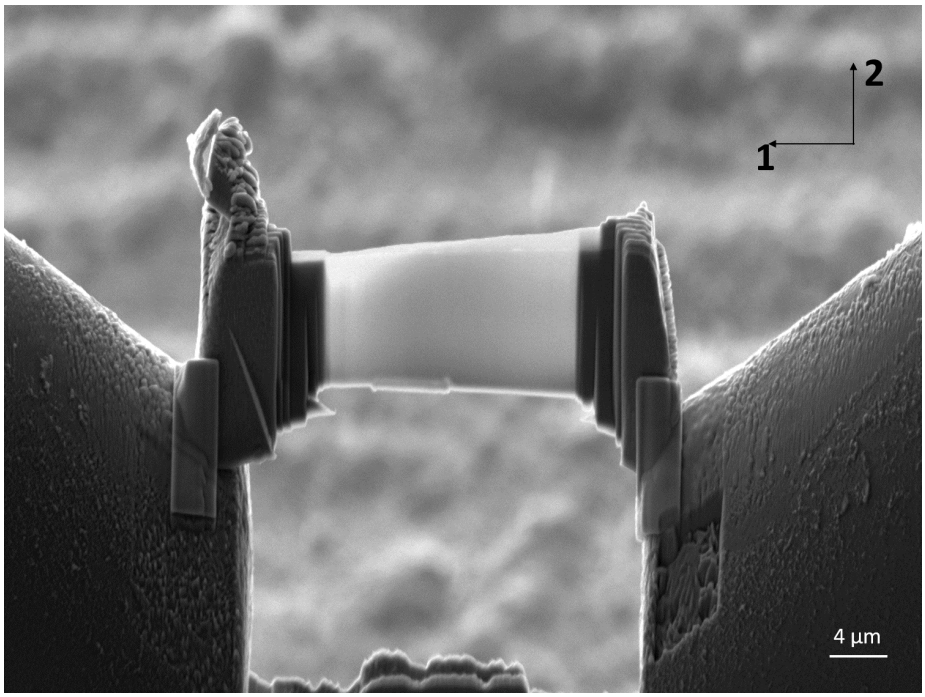

Figure 2: Sample S3 showing the thin sample for on-axis TKD measurement on the V-shaped post. Image acquired in the SEM 1nA@10kV using the In-lens detector.

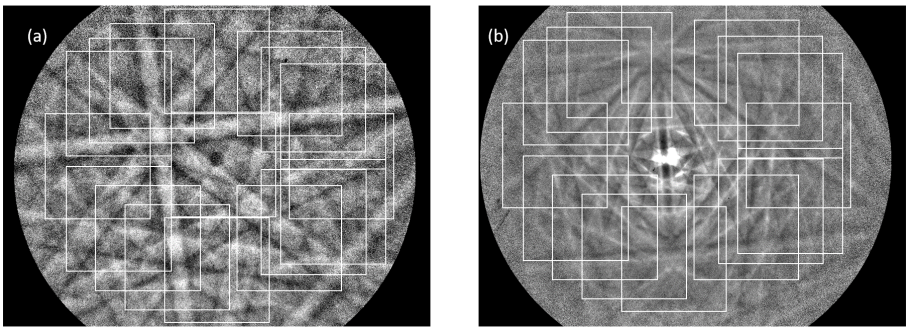

Figure 3: Patterns and ROIs (superimposed as white squares) from samples a) S1, obtained by EBSD and b) S3, obtained by on-axis TKD.

with the corresponding ROI selection is shown in Figure 3. Detailed description of the cross-correlation technique are discussed elsewhere [15, 28, 29]. The measured lattice rotations (and hence curvatures) are used to setup a Nye's tensor framework [30] to measure geometrically necessary dislocation (GND) density content. With 18 known dislocation types in this *fcc* phase and 6 lattice distortion gradients, we use an L^1 optimisation scheme to estimate dislocation content while minimising total dislocation line energy. More details on this have been presented by Wilkinson *et al.* [16].

Transmission electron microscopy images were obtained from the thin sample S3 using a JEOL 3000F TEM, operating at 200KeV to show the dislocation arrangement and make a comparison with the GND density maps obtained in the SEM.

3. Results and Discussion

EBSD and TKD maps across all the 4 samples were of the size approximately 22.5μm x 15μm and a step size of 50nm. These maps were then cropped to include most of the sample area and corrected for sample distortion arising from the drift during the EBSD map. The IPF maps (along direction '2') are shown below (before any drift corrections) in Figure 4 for all the samples. At the time taken to acquire patterns at sufficiently high resolution, the sample

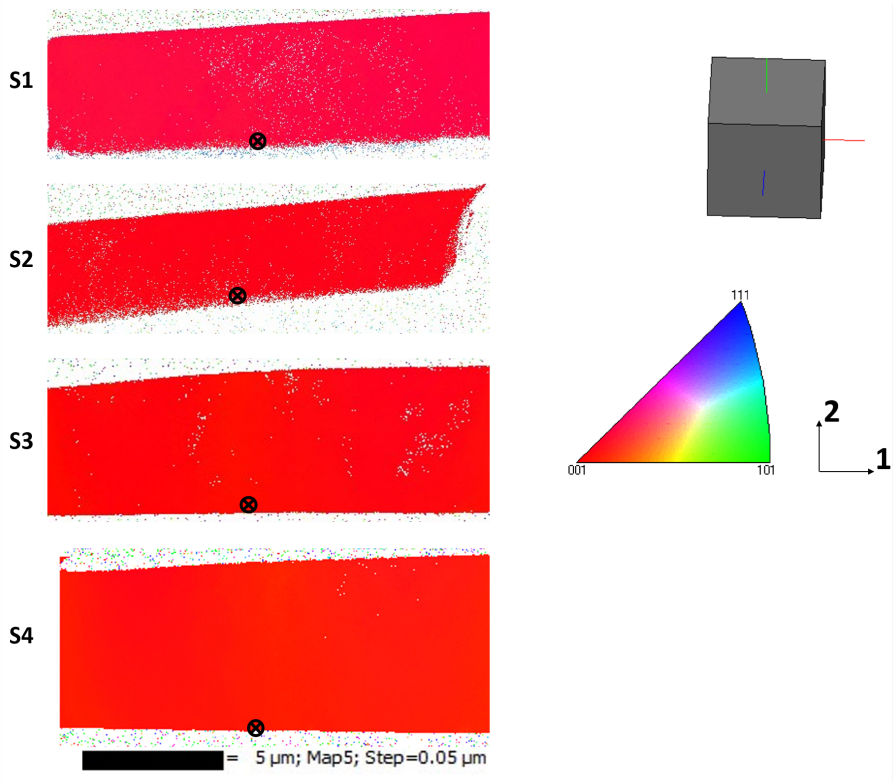

Figure 4: Inverse Pole Figure maps (IPF) along the direction '2'. The figure also shows the crystal orientation on the top-right. The black ⊗ symbol represents the reference point for each map.

drift in evident. The least amount of drift is observed in sample S3 and S4 (acquired in TKD). The maximum amount of drift is observed in sample S2, and from the strain/rotation maps it is evident that most of the area observed in the left of sample S1 has missed out due to the scan drift.

All the in-plane residual elastic strain maps of samples S1, S2, S3, S4 and lattice rotation ω_{13} around '2' axis are shown in Figures 5, 6, 7 and 8. The strains in sample S1 and S2 show relatively similar trends in tensile and compressive values. As already mentioned, most of the area to the left of sample S2 is lost due to scan drift, and the map roughly corresponds about 5μm to the right of where sample S1 is mapped. A suitable line scan comparison is described

later in Figure 10, to provide a better quantitative measurement than visual interpretation from color images. Slightly more noise may also be apparent in these scans, as a result of the surface being polished by FIB and not a traditional colloidal Silica or electropolished as is the case for general EBSD or HR-EBSD that is regularly followed. It should be noted that the surface was finished by a low KV FIB beam to minimise damage from the FIB and was left untouched after preparation for S1. The sample was thinned from the opposite side of the mapped area. These strains in the sample are the result of prior deformation in the sample during processing and are measured with respect to a reference point shown in Figure 4. A general concern that has been raised for elastic strain mapping in thin foils is that thinning may alter the elastic strains present as the stress across the free surfaces of the foil must drop to zero, and furthermore the foil might bend or twist out of plane during thinning. Our measurements in the foil sample S3 suggest that the changes in lattice strain are relatively small as stresses relax from thinning (see Figure 7). There is relatively more sample bending upon thinning further in sample S4, which gives rise to a change in magnitude of the strains (beyond a 20% difference). Also shown in Figure 7 and 8 is a map of the measured lattice rotation ω_{13}. With respect to the reference point in the centre of the sample (see Figure 4 for location of this reference point), it can clearly be seen that the sample rotates in an opposite sense on either side of the reference point going through a extreme rotation before rotating back to be close to the lattice orientation near the reference. This variation is stronger across the top of the maps, than the bottom. These lattice rotations are consistent with the foil being bent so that the vertical centre line is deflected somewhat out of the plane of the foil defined by the end posts of the omniprobe^{TM} grid. The ends of the foil are thus constrained from moving and instead the foil tends to bend during thinning.

To the right-side of the maps in samples S1 and S2, the area has values of strain and rotation very different from the left of the lamella. This does not appear to be a case of inconsistent cross-correlation evaluation or shadowing on the detector. The drop in the cross-correlation coefficient in this area is only

about 10% when compared to the rest of the sample area. The cross-correlation approach employed uses a very robust iterative weighing scheme to specifically prevent any outliner solutions for the individual ROIs.

It is also evident from sample S4 (Figure 8) that the strain measured by HR-TKD is influenced by the sample bending to a larger extent than sample S3. Since this sample was only prepared to check the sample bending from thinning, we do not discuss further about the results obtained in this study. The sample seems to bend even more than sample S3 as described above, around a vertical line in the center of the prepared foil. This makes the correction of the strains from a simple finite element model even more difficult and probably inaccurate.

From the strain maps for samples S1, S2 and S3, it can be seen that the tensile/compressive nature of the strain is still measured appropriately although with some lateral shifts due to sample drift during the EBSD scan time. The measured bending of the sample about the vertical '2' direction can be used to correct the measured strains. We only make this correction for the sample S3 that is appropriately prepared for regular TKD studies and thickness. For this purpose a finite element analysis (FEA) simulation was setup in ABAQUS. This setup was a simple 2-D three-point bend of a foil to match the curvature/bending of the measured sample S3 and resulting strains extracted to correct ϵ_{11}. A 2D sheet model was used with inbuilt controls and displacements imposed in the centre of the sheet (along axis '1') so as to cause sheet bending around the '2' direction. The displacement imposed was adjusted to cause a bending matched to the rotation ω_{13} in this experiment. The resulting strains are shown in Figure 9(a). It is presumed that these strains are lost due to sample bending and are hence used to correct the measurements. The correction term for ϵ_{11} at the centre (where it is predicted to be maximum), is in the order of 1×10^{-3}. The correction terms for the strains ϵ_{12} and ϵ_{22} based on this bending is in the order of 2×10^{-4} or lower and is thus ignored as this is lower than the sensitivity of the experimentally measured strains. The corrected ϵ_{11} map for sample S3 is shown in Figure 9(b). From the FEA simulation, the maximum deflection in bending in the centre of the sample is around 0.1μm for a sample 22μm x

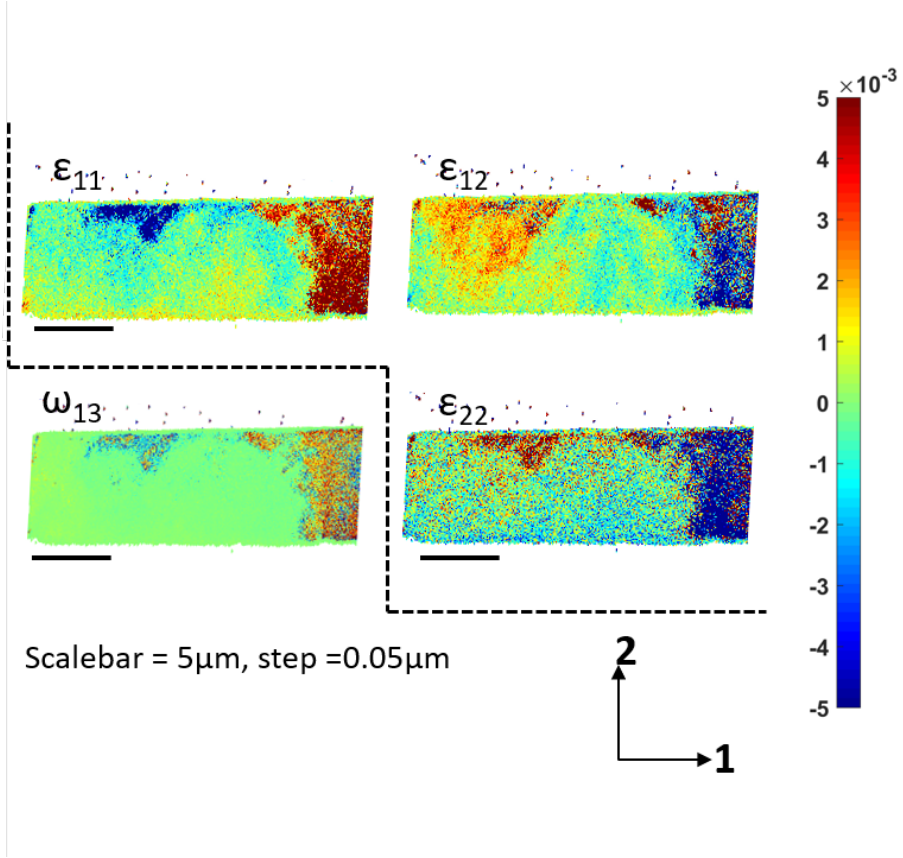

Figure 5: Residual elastic strain maps and Lattice Rotation map (around '2' direction) for sample S1. The upper and lower colour ranges (for strain and rotation (in radian)) denote $\pm 5 \times 10^{-3}$.

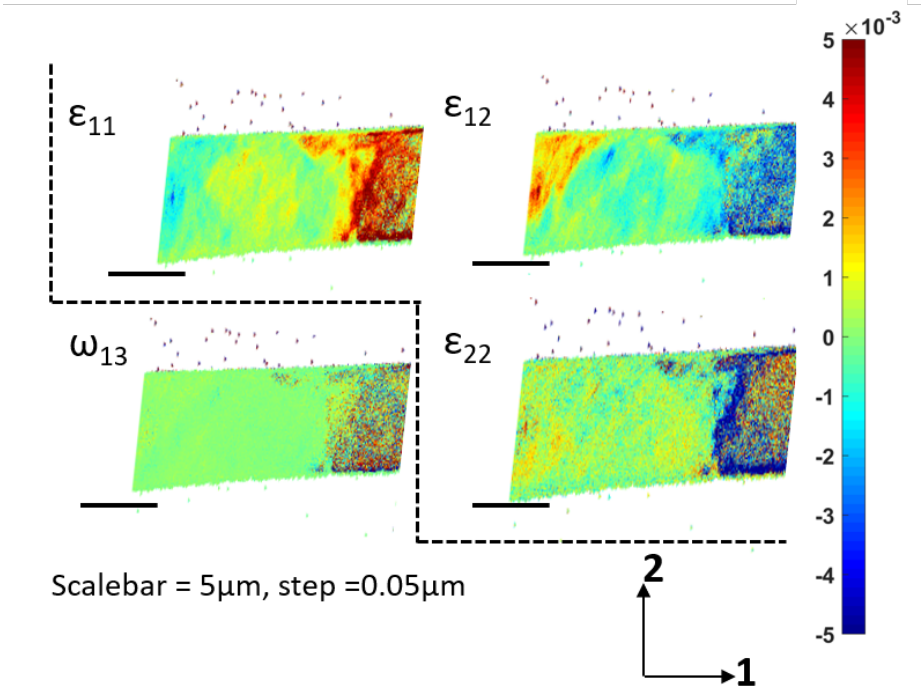

Figure 6: Residual elastic strain maps and Lattice Rotation map (around '2' direction) for sample S2. The upper and lower colour ranges (for strain and rotation (in radian)) denote $\pm 5 \times 10^{-3}$.

6μm. Such small bending may not always be possible to be picked up in the SEM/FIB during preparation, especially in this case when the bending is non-uniform in the sample area. In Figure 9(a), a deformation scale factor of 10 has been applied to show the visible bending.

For a qualitative comparison, a line profile for ϵ_{11} strain has been drawn across the 4 maps along a horizontal profile near the top of the map, where features can be observed in the stain maps. Data averaged across 10 pixels wide and gaussian smoothened is presented in Figure 10. This was done to evenly compare similar lines across the 4 samples. The error bars depict the standard deviation of the strain variation within the 10 pixel width. Elastic stresses can be calculated by using Hooke's law to write them in terms of elastic strain and

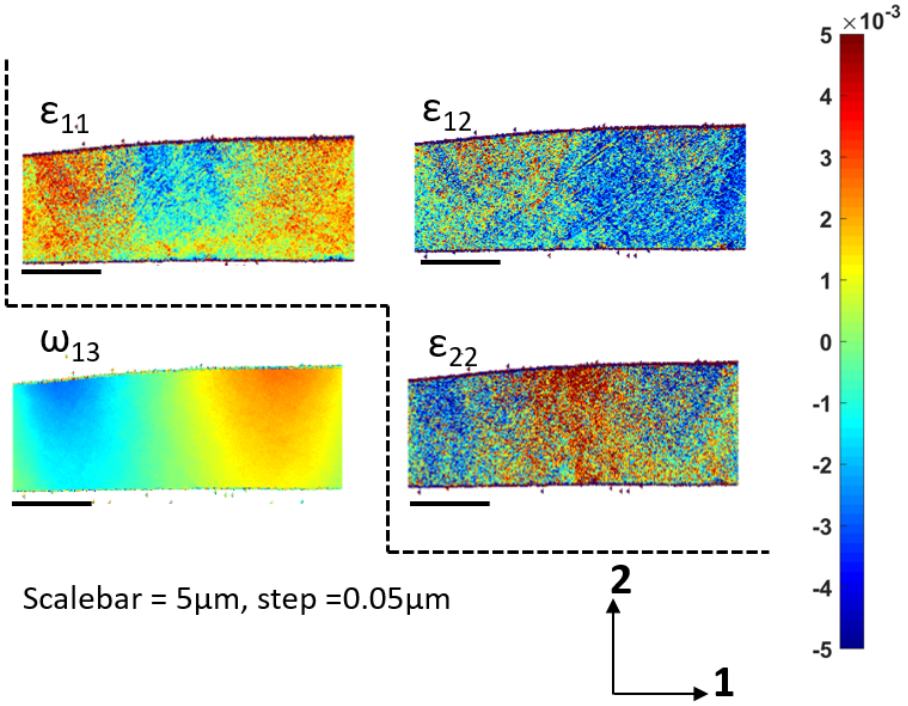

Figure 7: Residual elastic strain maps and Lattice Rotation map (around '2' direction) for sample S3. The upper and lower colour ranges (for strain and rotation (in radian)) denote $\pm 5 \times 10^{-3}$.

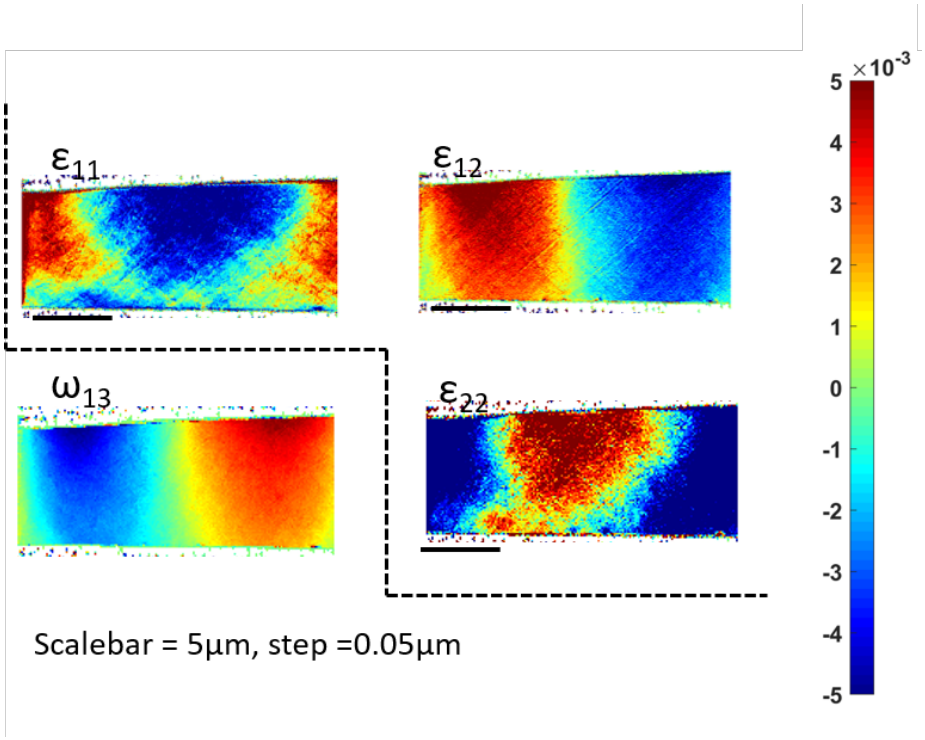

Figure 8: Residual elastic strain maps and Lattice Rotation map (around '2' direction) for sample S4. The upper and lower colour ranges (for strain and rotation (in radian)) denote $\pm 5 \times 10^{-3}$.

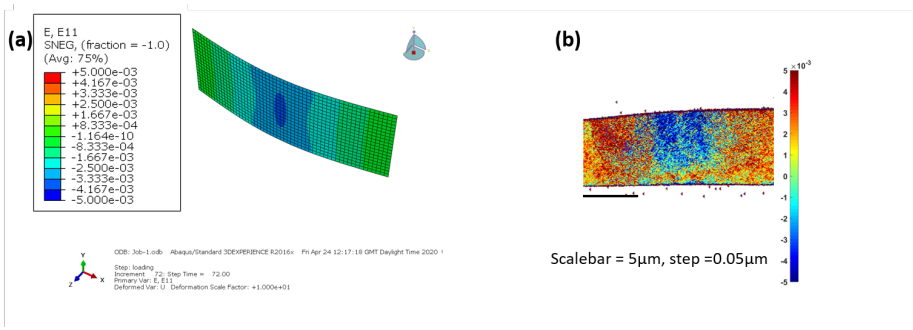

Figure 9: a) Strains ϵ_{11} from the Abaqus simulation model used for correction (the deformation has been amplified by a scale factor of 10 to show visible bending) and the upper and lower ranges depicted are between $\pm \times 10^{-3}$, b) Corrected residual elastic strain maps (after accounting for sample bending) for sample S3. The upper and lower ranges denote $\pm 5 \times 10^{-3}$.

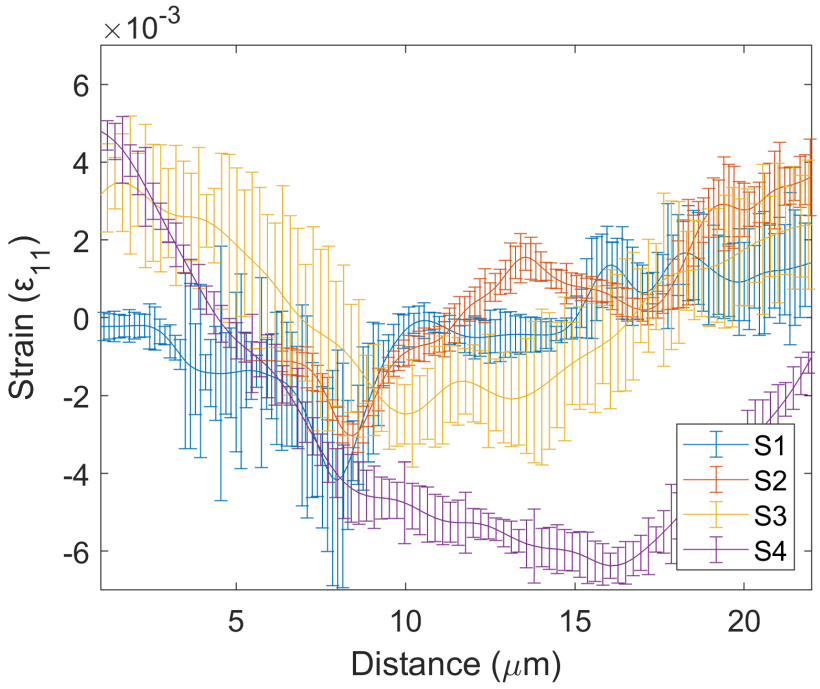

Figure 10: Line profile variation of ϵ_{11} strains in samples S1, S2, S3 (after correction) and S4.

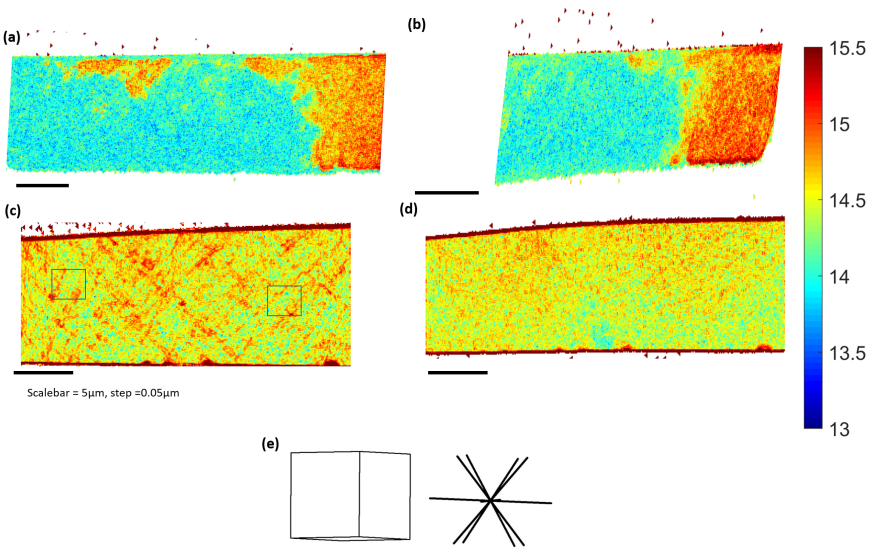

Figure 11: GND Density (in logarithmic scale of $lines/m^2$) maps of the sample a) S1, b) S2, c) S3 (the areas marked in blue squares are examined in the TEM in Figure 12) and d) S4. e) Crystal orientation and the trace of the $\langle 1\,1\,0 \rangle$ direction are depicted for the sample.

know elastic stiffness constants. For comparison with the strain and to estimate the magnitude of the stresses, the elastic stress tensor maps for samples S1 and S3 are shown in Appendix A.

Perhaps the most striking part of this work is the GND density maps produced from measured lattice rotations, shown in Figure 11. For samples S1 and S2, most of the GND concentration appears to be in the area that has a relatively higher measured strain component. Without correcting for the sample bending, the GNDs measurements appears to be elevated along the trace of the $\langle 1\,1\,0 \rangle$ slip direction in the sample S3.

Also shown are two TEM images from the sample S3 (marked by square regions in Figure 11(c)), to the left and right area of the map depicting dislocation arrangements in these areas. It can be clearly seen that the dislocations lie on the $\langle 1\,1\,0 \rangle$ traces. In the location marked in Figure 12(a), there are about 30 dislocations in a 0.5 x 0.5 μm^2 area. This corresponds to a dislocation density of

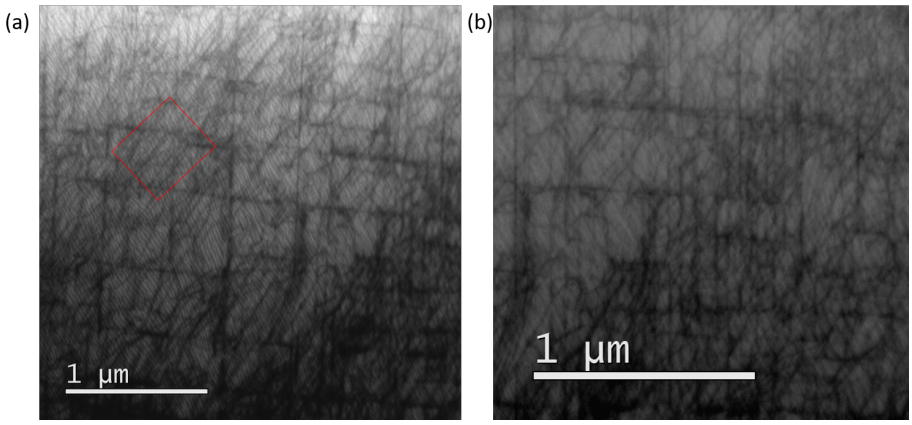

Figure 12: TEM images from the marked areas in Figure 11(c) to the (a)left and (b)right of the TKD map. An area is marked in red to estimate the dislocation density.

$1.2 \times 10^{14} lines/m^2$. This is roughly consistent with the GND density estimated from TKD of $3.9 \times 10^{14} lines/m^2$.

To illustrate that the GND density measurements are fairly consistent throughout the experiment, a mean (in $lines/m^2$) with a standard deviation are provided here. It should be noted that the spatial distribution of the measured GND values is quite varied in the area and thus results in a larger standard deviation. The initial mean GND density in the sample S1, as measured by HR-EBSD was found to be $2.2 \times 10^{14} \pm 2.5 \times 10^{14}$. In the sample S2, as measured by HR-EBSD, the mean was $3.02 \times 10^{14} \pm 3.5 \times 10^{14}$. After thinning and measurement via HR-TKD, the mean GND value on sample S3 was found to be $1.8 \times 10^{14} \pm 7.7 \times 10^{13}$. In the very thin sample S4, the mean GND value was found to be $3.9 \times 10^{14} \pm 6.1 \times 10^{14}$.

4. Conclusions

The on-axis TKD type of analysis can provide strain and GND measurements with much superior spatial resolution than EBSD or even off-axis TKD. The step size used for all the maps in this paper, 50nm, was however chosen close to the spatial resolution limit of regular EBSD in samples S1 and S2, for a

meaningful comparison between techniques. On samples where measurements are necessary at step sizes less than 50nm and in cases where sample drift may be an issue, on-axis HR-TKD offers a much better alternative to HR-EBSD. The time required for the on-axis TKD map (at the same pattern resolution) for samples S3 and S4, when compared to the samples S1 and S2 was quicker by over 5 times.

Care must be taken when preparing samples for TKD to minimise sample bending and shadowing. In some other work done on similar samples, some issues were encountered when it comes to acquiring patterns. Uneven FIB thinning in some cases seems to cause a contrast inversion in the Kikuchi patterns.

In cases when the sample surface is inaccessible for traditional polishing techniques and EBSD, a FIB liftout can be prepared and a cross-correlation analysis of these patterns (HR-TKD) to measure elastic strains, lattice rotation and GND density is possible. As we have presented in this paper, the elastic strains as a result of sample thinning do not relax completely. From the thinning during the FIB preparation and measured sample bending in a constrained sample, this relaxed strain corresponds to $\sim 1 \times 10^{-3}$ in the central portion of the sample. To put this into a general perspective, it corresponds to a loss of about 20% in strain from the thick sample. The relaxation however may not be uniform due to the constrains at the ends. From experience, an unconstrained sample welded to a post on only one side seems to cause much more visible sample bending and in majority of cases unable to acquire clear patterns from a flat sample and additional shadowing from the post. This may result in much more stress relaxation, and strain redistribution than the configuration used by the authors in this paper. By selecting a reference pattern from the central region of the sample, this information from relaxation is often lost from the strain maps, but can however be clearly observed in the lattice rotation measured. The relaxation thus reduces the strains in the sample manifested as sample bending, but this can be corrected in some cases. This has also been shown in a previous work by the authors, although at a much smaller step size, where the strain fields have been measured around finer microstructural features

[22] and these measurements compared to simulations [19, 26].

We have found that strain and GND densities measured by HR-TKD on thin samples seem to be representative of those in the bulk when the right care is taken on the sample preparation and on the choice of parameters for the acquisition and provided with a quantitative comparison. An ideal sample thickness for HR-TKD based measurements seems to be in the order of 130nm or slightly higher.

5. Acknowledgements

The EPSRC (EP/K040375/1, EP/N010868/1 and EP/R009392/1) grants are acknowledged for funding this research. The authors acknowledge use of characterisation facilities within the David Cockayne Centre for Electron Microscopy, Department of Materials, University of Oxford, alongside financial support provided by the Henry Royce Institute (Grant ref EP/R010145/1). The authors would also like to thank EDF R&D, Avenue des Renardieres for providing the sample.

6. Appendix A

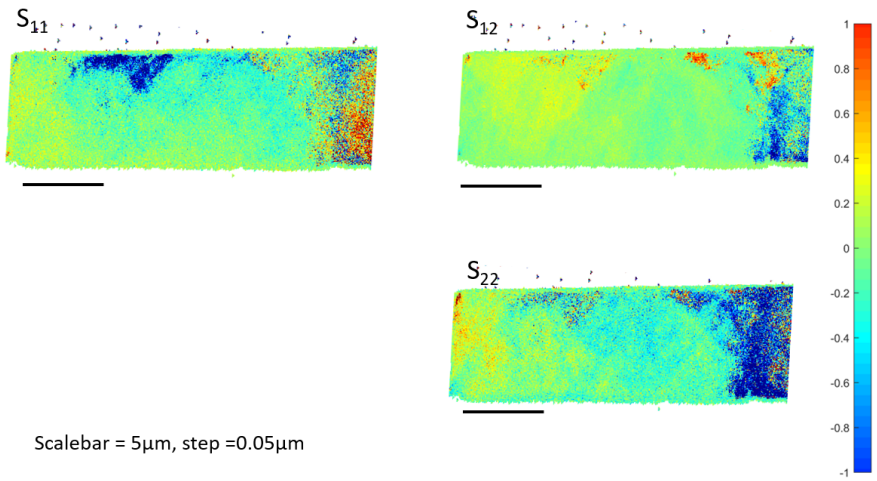

Figure 13: Residual elastic stress maps for sample S1. The upper and lower colour ranges denote ±1 GPa.

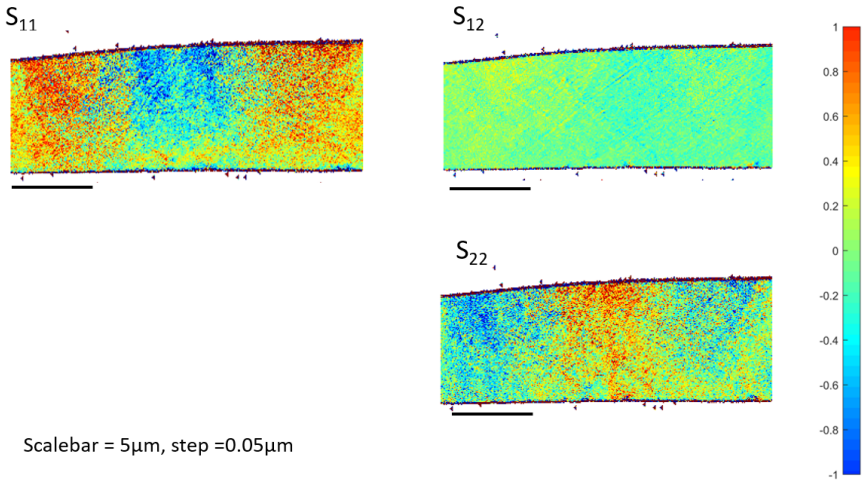

Figure 14: Residual elastic stress maps for sample S3. The upper and lower colour ranges denote ±1 GPa.

References

[1] A. J. Wilkinson, P. B. Hirsch, Electron diffraction based techniques in scanning electron microscopy of bulk materials, Micron 28 (4) (1997) 279

– 308. doi:10.1016/S0968-4328(97)00032-2.

[2] D. P. Field, Recent advances in the application of orientation imaging, Ultramicroscopy 67 (1) (1997) 1 – 9, frontiers in Electron Microscopy in Materials Science. doi:10.1016/S0304-3991(96)00104-0.

[3] F. J. Humphreys, Grain and subgrain characterisation by electron backscatter diffraction, Journal of Materials Science 36 (2001) 3833–3854. doi:10.1023/A:1017973432592.

[4] V. Randle, Application of electron backscatter diffraction to grain boundary characterisation, International Materials Reviews 49 (1) (2004) 1–11. doi:10.1179/095066004225010514.

[5] A. J. Schwartz, M. Kumar, B. L. Adams, D. P. Field, Electron backscatter diffraction in materials science, Springer US, 2009. doi:10.1007/978-0-387-88136-2.

[6] A. J. Wilkinson, T. B. Britton, Strains, planes, and ebsd in materials science, Materials Today 15 (9) (2012) 366 – 376. doi:10.1016/S1369-7021(12)70163-3.

[7] K. Z. Troost, P. Vandersluis, D. J. Gravesteijn, Microscale Elastic-Strain Determination by Backscatter Kikuchi Diffraction in the Scanning Electron-Microscope, Applied Physics Letters 62 (10) (1993) 1110–1112. doi:10.1063/1.108758.

[8] A. J. Wilkinson, Measurement of elastic strains and small lattice rotations using electron back scatter diffraction, Ultramicroscopy 62 (4) (1996) 237–247. doi:10.1016/0304-3991(95)00152-2.

[9] T. Tanaka, A. J. Wilkinson, Pattern matching analysis of electron backscatter diffraction patterns for pattern centre, crystal orientation and absolute elastic strain determination – accuracy and precision assessment, Ultramicroscopy 202 (2019) 87–99. doi:10.1016/j.ultramic.2019.04.006.

[10] T. Vermeij, J. P. Hoefnagels, A consistent full-field integrated DIC framework for HR-EBSD, Ultramicroscopy 191 (2018) 44–50. doi:10.1016/j.ultramic.2018.05.001.

[11] J. Alkorta, M. Marteleur, P. J. Jacques, Improved simulation based HR-EBSD procedure using image gradient based DIC techniques, Ultramicroscopy 182 (2017) 17–27. doi:10.1016/j.ultramic.2017.06.015.

[12] S. Kalácska, Z. Dankházi, G. Zilahi, X. Maeder, J. Michler, P. D. Ispánovity, I. Groma, Investigation of geometrically necessary dislocation structures in compressed Cu micropillars by 3-dimensional HR-EBSD, Materials Science and Engineering A 770 (2020) 138499. doi:10.1016/j.msea.2019.138499.

[13] J. Kacher, C. Landon, B. L. Adams, D. Fullwood, Bragg's Law diffraction simulations for electron backscatter diffraction analysis, Ultramicroscopy 109 (9) (2009) 1148–1156. doi:10.1016/j.ultramic.2009.04.007.

[14] C. Maurice, J. H. Driver, R. Fortunier, On solving the orientation gradient dependency of high angular resolution EBSD, Ultramicroscopy 113 (2012) 171–181. doi:10.1016/j.ultramic.2011.10.013.

[15] T. B. Britton, A. J. Wilkinson, High resolution electron backscatter diffraction measurements of elastic strain variations in the presence of larger lattice rotations, Ultramicroscopy 114 (2012) 82–95. doi:10.1016/j.ultramic.2012.01.004.

[16] A. J. Wilkinson, D. Randman, Determination of elastic strain fields and geometrically necessary dislocation distributions near nanoindents using electron back scatter diffraction, Philosophical Magazine 90 (9) (2010) 1159–1177. doi:10.1080/14786430903304145.

[17] R. R. Keller, R. H. Geiss, Transmission EBSD from 10 nm domains in a scanning electron microscope, Journal of Microscopy 245 (3) (2012) 245–251. doi:10.1111/j.1365-2818.2011.03566.x.

[18] P. W. Trimby, Orientation mapping of nanostructured materials using transmission Kikuchi diffraction in the scanning electron microscope, Ultramicroscopy 120 (2012) 16–24. doi:10.1016/j.ultramic.2012.06.004.

[19] H. Yu, J. Liu, P. Karamched, A. J. Wilkinson, F. Hofmann, Mapping the full lattice strain tensor of a single dislocation by high angular resolution transmission Kikuchi diffraction (HR-TKD), Scripta Materialiadoi:10.1016/j.scriptamat.2018.12.039.

[20] J. J. Fundenberger, E. Bouzy, D. Goran, J. Guyon, H. Yuan, A. Morawiec, Orientation mapping by transmission-SEM with an on-axis detector, Ultramicroscopy 161 (2016) 17–22. doi:10.1016/j.ultramic.2015.11.002.

[21] F. Niessen, A. Burrows, A. B. d. S. Fanta, A systematic comparison of on-axis and off-axis transmission Kikuchi diffraction, Ultramicroscopy 186 (2018) 158–170. doi:10.1016/j.ultramic.2017.12.017.

[22] Y. T. Tang, P. Karamched, J. Liu, J. C. Haley, R. C. Reed, A. J. Wilkinson, Grain boundary serration in nickel alloy inconel 600: Quantification and mechanisms, Acta Materialia 181 (2019) 352–366. doi:10.1016/j.actamat.2019.09.037.

[23] J. Liu, S. Lozano-Perez, A. J. Wilkinson, C. R. Grovenor, On the depth resolution of transmission Kikuchi diffraction (TKD) analysis, Ultramicroscopy 205 (2019) 5–12. doi:10.1016/j.ultramic.2019.06.003.

[24] Z. Shen, K. Arioka, S. Lozano-Perez, A mechanistic study of SCC in Alloy 600 through high-resolution characterization, Corrosion Science 132 (2018) 244–259. doi:10.1016/j.corsci.2018.01.004.

[25] N. Saravanan, P. S. Karamched, J. Liu, C. Rainasse, F. Scenini, S. Lozano-Perez, Using local gnd density to study scc initiation, Ultramicroscopy 217 (2020) 113054. doi:https://doi.org/10.1016/j.ultramic.2020.113054.

[26] Y. Xu, S. Joseph, P. Karamched, K. Fox, D. Rugg, F. P. E. Dunne, D. Dye, Predicting dwell fatigue life in titanium alloys : Modelling and experiment, Nature Communications (11) (2020) 5868. doi:https://doi.org/10.1038/s41467-020-19470-w.

[27] S. F. Bordín, S. Limandri, J. Ranalli, G. Castellano, Ebsd spatial resolution for detecting sigma phase in steels, Ultramicroscopy 171 (2016) 177 – 185. doi:https://doi.org/10.1016/j.ultramic.2016.09.010.

[28] A. J. Wilkinson, D. J. Dingley, G. Meaden, Strain mapping using electron backscatter diffraction (2009). doi:10.1007/978-0-387-88136-2_17.

[29] A. J. Wilkinson, G. Meaden, D. J. Dingley, High resolution mapping of strains and rotations using electron backscatter diffraction, Materials Science and Technology 22 (11) (2006) 1271–1278. doi:Doi10.1179/174328406x130966.

[30] J. F. Nye, Some geometrical relations in dislocated crystals, Acta Metallurgica 1 (2) (1953) 153–162. doi:10.1016/0001-6160(53)90054-6.